IEEE Access
Multidisciplinary | Rapid Review | Open Access Journal

Received 22 May 2023, accepted 7 June 2023, date of publication 5 July 2023, date of current version 12 July 2023.

Digital Object Identifier 10.1109/ACCESS.2023.3292529

RESEARCH ARTICLE

A Double Layer Cross-Slot Aperture-Fed Millimeter-Wave Antenna Array With Wide Axial Ratio Bandwidth

MAHARANA PRATAP SINGH[1], (Graduate Student Member, IEEE), JIRO HIROKAWA[2], (Fellow, IEEE), AND SAPTARSHI GHOSH[1], (Senior Member, IEEE)

[1]Department of Electrical Engineering, Indian Institute of Technology Indore, Indore, Madhya Pradesh 453552, India
[2]Department of Electrical and Electronic Engineering, Tokyo Institute of Technology, Tokyo 1528552, Japan

Corresponding author: Maharana Pratap Singh (maharana@ieee.org)

This work was supported in part by the Department of Science and Technology (DST) under Project DST/INT/JSPS/P-329/2021, and in part by the Japan Society for the Promotion of Science (JSPS) under Project JPJSBP 120217704.

ABSTRACT This letter presents a double-layer cross-slot aperture-fed antenna array with wide axial ratio bandwidth for 5G millimeter-wave applications. Each of the antenna elements comprises two parasitic trapezoid patches and three suspended metallic vias, which are excited through an aperture coupling technique with the help of a cross-slot geometry. Two circularly polarized (CP) resonances are produced by each antenna, yielding an overall wideband CP behavior upon optimization. Superior performances are thereby observed from the antenna element in terms of a wide 3-dB axial ratio bandwidth (ARBW) of 26.38%, a wide -10 dB impedance bandwidth $>$ 31.40%, and a large gain (5.6 $\pm$ 1.0 dBic) in the broadside direction. To further improve the characteristics, a 1 $\times$ 4 antenna array is devised using a corporate feed network, which exhibits an extensive ARBW of 30.34%, a broadband impedance bandwidth $>$33.33%, and an increased gain of 11.2 $\pm$ 1.0 dBic. Both the single element and antenna array are fabricated, and their measured responses are in reasonable agreement with the simulated results.

INDEX TERMS Aperture-fed, axial ratio bandwidth (ARBW), antenna array, fifth-generation (5G), millimeter-wave (mm-wave).

I. INTRODUCTION

Owing to the expeditious expansion of 5th generation (5G) and future wireless communication for serving the requirement of tremendously high data rate and large bandwidth in various real-time applications, the carrier frequency of the communication system in the present time has been slowly shifting towards the millimeter-wave (mm-wave) spectrum [1], [2], [3]. Although mm-wave frequency has manifold advantages, attenuation of the signal at these regimes is much more severe due to significant propagation loss. To deal with this concern, array networks are often designed with enhanced gain and high directivity [4], [5]. In recent years, several printed monopoles and substrate integrated waveguide (SIW) based cavity-backed linearly polarized (LP) antennas have been reported [6], [7], [8]. But a circularly polarized (CP) antenna, in contrast, has widespread applications due to its superiority as compared to its LP counterpart [9], [10]. It can efficiently handle environmental obstacles such as multipath interference, Faraday rotation, and inclement weather conditions [11], [12], [13], [14], as well as can provide freedom from the inclination between transmitting and receiving antennas without affecting the received signal strength [15]. A mm-wave CP antenna is therefore much needed for 5G applications.

Attracted by various unique features, several mm-wave CP antennas have recently been introduced exhibiting different characteristics [16], [17], [18], [19], [20], [21], [22], [23], [24], [25]. A single-layer end-fire SIW-based antenna is made from the combination of a Vivaldi antenna and a planar horn antenna to realize an axial ratio (AR) of 8.87% [16]. Another single-layer omnidirectional CP antenna is

The associate editor coordinating the review of this manuscript and approving it for publication was Davide Ramaccia.

demonstrated in [17], showing an 8.00% AR bandwidth. Reference [18] presents a dielectric resonator loaded SIW-based three-layered slot antenna, which exhibits an AR bandwidth (ARBW) of 15.60%. A stepped slot-type mm-wave antenna using a SIW feeding network is designed at 37.5 GHz with 22.50% ARBW [19]. In [20], an end-fire antipodal tapered slot antenna is demonstrated at 28 GHz with an ARBW of 5.00%. In [21], a microstrip line and square patch based RHCP four-layered slot antenna is reported at 28 GHz with an ARBW of 8.42% and a peak gain of 11.65 dBic. A magneto-electric dipole element has been used to realize a three-layered mm-wave antenna, whose 2×2 array displays an ARBW of 11.33%, and a maximum gain of 13.12 dBic [22]. However, most of the available single and double-layered mm-wave antennas have limited ARBWs or/and inadequate gains. The performances may further be enhanced either by increasing the number of substrate layers (thereby generating complicated fabrication problems, such as alignment issues, creating numerous metallic vias, bonding layer effects, etc.) or by using intricate designs. Therefore, wideband mm-wave CP antennas with commendable performances at the expense of using a limited number of substrate layers and simple design procedures are still in dire need.

In this letter, a double-layered wideband CP antenna array is designed and demonstrated for 5G communication, while aiming to resolve the above bottlenecks. The proposed geometry design is made of amalgamating multiple innovative techniques while getting rid of complicated fabrication methods and intricate design procedures. It has two substrate layers; the bottom layer is used for aperture couple feeding, and the top layer is used for CP generation. The conventional printed circuit board (PCB) technique has been used to realize the antenna geometries, thereby having the potential to further enhance the antenna performance, if needed. A combination of metallic patches, slots, and vias are intelligently exploited in the topology to result in wideband CP behavior, large impedance bandwidth, and high directivity. A 1×4 simple corporate feed network is later used to further improve the antenna performance, while keeping the design complexity into a lower limit. A detailed equivalent circuit model is also devised to explain the antenna operation. The measured responses confirm the proposed concept and its usability for 5G applications.

The remaining parts of the paper are organized in the following ways. Section II explains the design, operating mechanism, equivalent circuit model, and parametric study of the antenna element. Section III elaborates the antenna array configuration along with its simulated and measured results. Lastly, a conclusion is presented in Section IV.

II. ANTENNA ELEMENT ANALYSIS AND DESIGN

A. ANTENNA CONFIGURATION

The geometry of the proposed double-layer wideband CP antenna element is depicted in Fig. 1. The structure is made of two substrate layers; the top substrate consists of multiple metallic patterns and vias, whereas the bottom dielectric is used to feed the geometry for wideband operation. Two trapezoidal patches are printed on the top side and two unequal length orthogonal slots inclined at $\pm 45°$ are etched on the bottom side of the upper substrate. Three metallic vias are engraved across the upper substrate at appropriate positions. A 50 Ω feed line is designed on the bottom side of the lower substrate such that the signal gets coupled from the bottom layer microstrip feed to the top layer radiating patch through the cross-slot geometry. Rogers 5880 (TM) having a relative permittivity of 2.2 and a loss tangent of 0.0009 is used as the constituent substrate in both layers, whereas 17 μm copper is used as the metal claddings. The upper and lower dielectrics have different heights, viz. 0.786 mm and 0.254 mm, respectively. The other dimensions of the geometry are mentioned in the caption of Fig. 1.

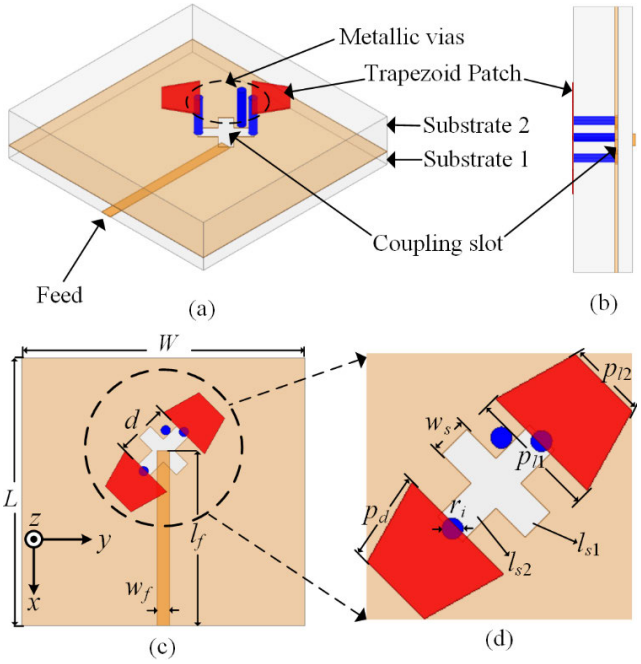

FIGURE 1. Geometry of the proposed wideband CP single antenna. (a) Perspective view, (b) side view, (c) top view of top layer, and (d) zoomed view. The optimized dimensions are: $W = 14$, $L = 15$, $l_f = 11.1$, $w_f = 0.8$, $l_{s1} = 3.35$, $l_{s2} = 3.7$, $w_s = 1.1$, $r_i = 0.2$, $P_{l1} = 3.7$, $P_{l2} = 2.3$, $p_d = 2.31$, and $d = 3.4$ (units: mm).

B. CP GENERATION MECHANISM

To realize the CP radiation, two orthogonal field components with 90^o phase difference are required. A step-by-step design methodology is illustrated in Fig. 2 exhibiting the occurrence of such criteria in different frequencies. A simple cross-slot geometry with unequal length could generate circularly polarized radiation by generating two orthogonal field components [26]. Hence in the initial design (Ant 1), a cross slot is etched above a feedline. This not only assists in coupling the energy from the feedline to the structure above by aperture coupling, but also produces a narrow-band CP radiation at 28 GHz upon optimization of the slot dimensions. It is also observed that if

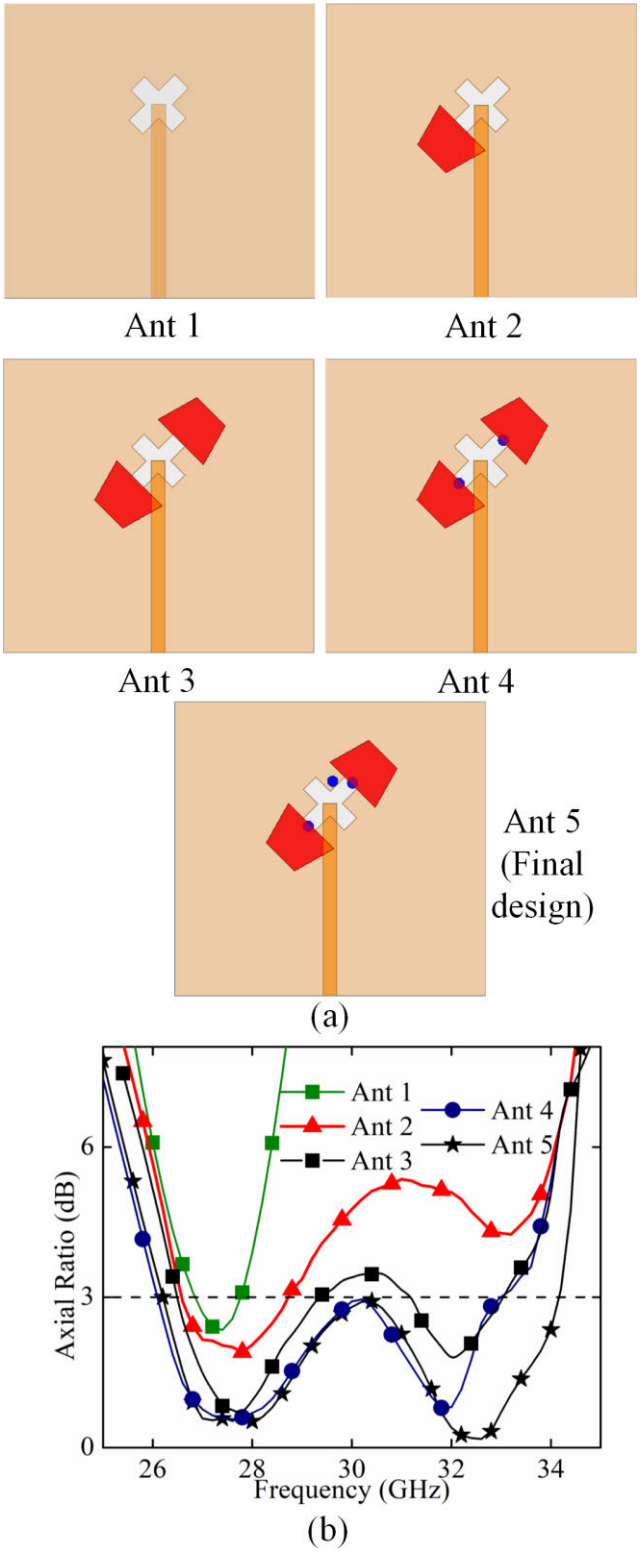

FIGURE 2. Transitional designs explaining CP mechanism: (a) design methodology, and (b) corresponding AR responses.

an asymmetrical patch or multiple parasitic dipoles are placed in a titled condition above a slot geometry, a CP radiation can be generated [27]. A polygon has multiple sides and by

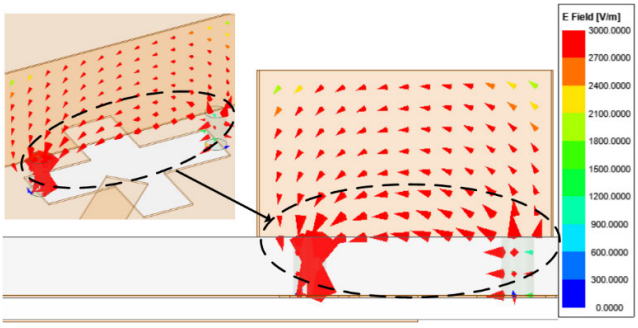

FIGURE 3. Electric field vector distribution in a vertical sheet (perpendicular to *xy*-plane) showing the contribution of metallic vias at 32 GHz.

adding appropriate tilt angles to the polygon, a phase shift can be introduced between the two perpendicular electric field components, thereby generating the CP resonance. A simple trapezoidal patch is thereafter chosen above the cross slot as shown in Ant 2. The patch is placed at the location above one end of the cross-slot where the radiating patch experiences maximum coupling with the electromagnetic (EM) wave. This configuration introduces a new CP response at around 33 GHz, in addition to the existing CP behavior at 28 GHz, as shown in Fig. 2(b). However, the axial ratio performance is poor at 33 GHz. To achieve a wider ARBW, a symmetrical patch is added at the diametrically opposite side of the slot in the next design (Ant 3). This additional patch generates an electric field circulating between the two patches, improving the axial ratio performance and polarization purity at 33 GHz. Two distinct CP resonances are achieved, but the axial ratio at intermediate frequencies (around 30 GHz) remains slightly greater than 3 dB. It is observed that two metallic posts separated by a certain distance could act as an electric dipole while placed inside an EM field [27]. The E-field generated by the dipole can combine with neighboring E-fields and can subsequently improve the CP performance. Two metallic vias are thereafter inserted across the upper substrate connecting the trapezoidal patches with the slot edges, as shown in Ant 4. This pair of metal posts acts as a strip dipole (with opposite charge distributions at each post) and generate an E-field parallel to the ground plane at 32 GHz, as evident from Fig. 3. This E-field propagates in two orthogonal directions on the top patches and bottom cross-slot, and the CP response at higher frequency gets significantly improved, as observed in Fig. 2(b). In the final geometry (Ant 5), one more metallic via is added to further enhance the antenna CP performance. Consequently, a wide ARBW covering from 26.20 to 34.16 GHz (corresponding to a fractional bandwidth of 26.38%) has been achieved. Thus the proposed design exploits two different concepts (viz. a cross-slot of unequal length and a pair of trapezoidal patch geometry) to realize two distinct CP characteristics, one at 28 GHz and another at around 32 GHz, and three metallic vias are subsequently added to improve the CP behavior as well as operating bandwidth.

The surface current distribution has also been investigated to study the CP operation in different time phases, as depicted

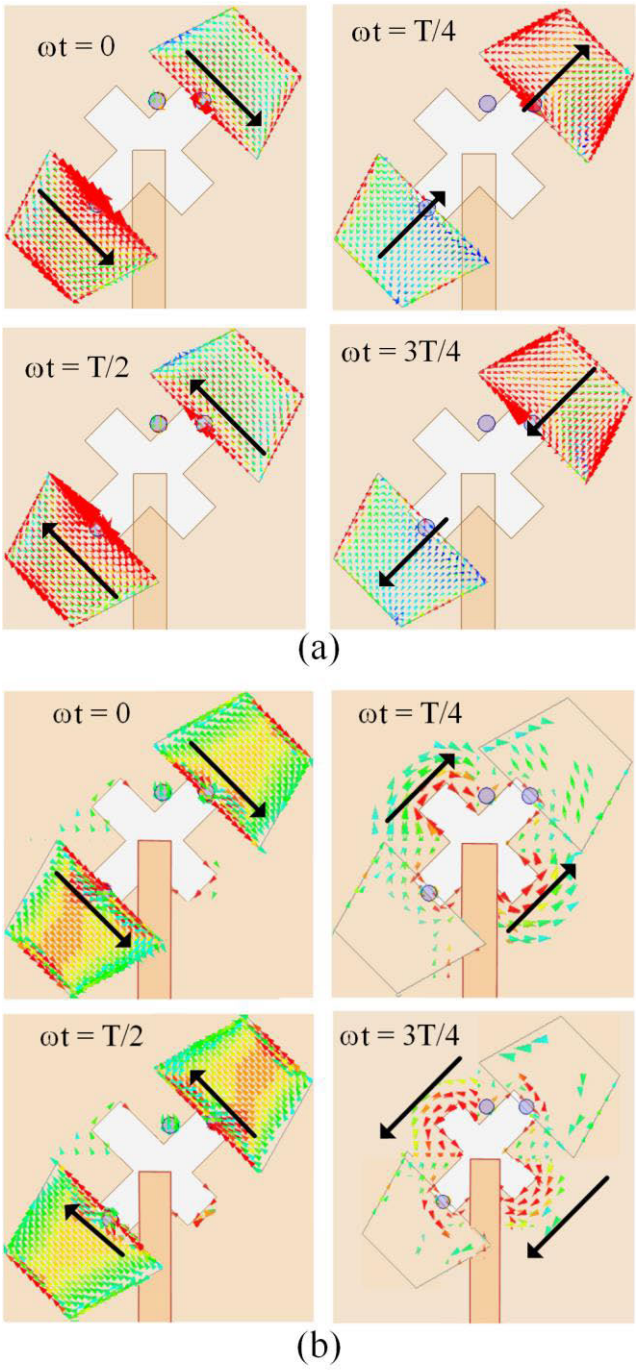

FIGURE 4. Surface current distribution in the proposed antenna showing RHCP behavior at (a) 28 GHz, and (b) 32 GHz.

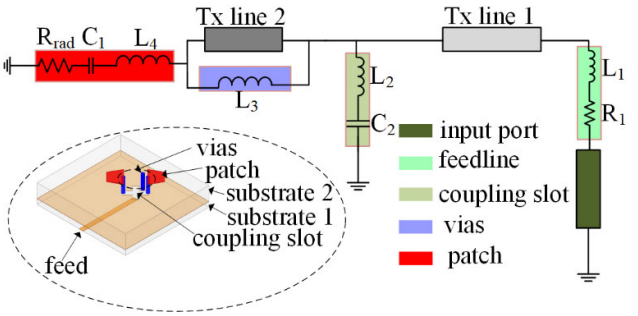

FIGURE 5. The equivalent circuit model of the proposed antenna element.

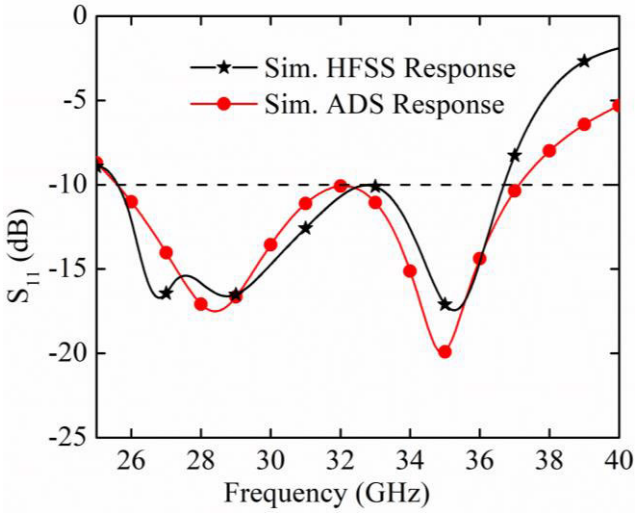

FIGURE 6. Comparison between the simulated results of the HFSS and equivalent circuit model.

in Fig. 4. Fig. 4(a) represents surface current at 28 GHz, which reveals that at zero time instant ($\omega t = 0$), both the trapezoidal patches contribute the surface current towards $-45°$ angle. At $\omega t = T/4$, the current on both the patches is directed towards $+45°$ angle. Surface currents at $\omega t = T/2$ and 3T/4 are generated in similar and opposite fashions to the previous two cases. Thus, the current rotates in a counter-clockwise direction, resulting in a right-hand CP (RHCP) behavior at 28 GHz. Surface current at 32 GHz is also depicted in Fig. 4(b). The figure shows, at $\omega t = 0$ time instant, both the trapezoidal patches contribute the surface current towards $-45°$ angle. This current is generated due to the coupling between the suspended metallic vias and the patch geometries placed above them. At $\omega t = T/4$ time phase, most of the induced surface current is circulating from one patch to another with the help of the cross-slot geometry. This induced current is due to the suspended metallic vias acting as the strip dipole and generates E-field along the length joining the dipole. Hence an effective current is generated at $+45°$ direction at this time phase. Thus, the overall response is obtained as a right-hand CP (RHCP) behavior at 32 GHz, where both the patches and strip metallic dipole are contributing toward the surface currents. By optimizing the dimensions and positions of the metallic vias near the slots, the AR level is maintained below 3 dB level between the two resonances, and a wideband CP performance is overall achieved.

C. EQUIVALENT CIRCUIT MODELING

A detailed equivalent circuit model is devised in Fig. 5 for the proposed antenna element to further explain its operating principle. The feedline is represented by a series combination

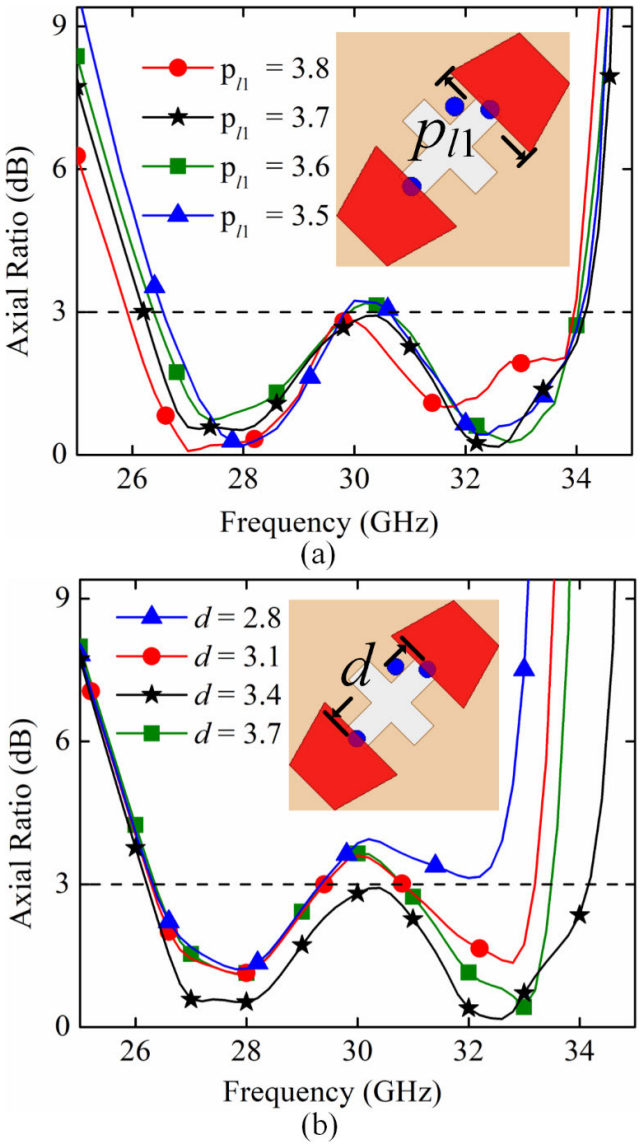

FIGURE 7. Simulated AR for different values of (a) p_{l1} and p_{l2} (varying in similar ratio) and (b) d in the proposed antenna (units: mm).

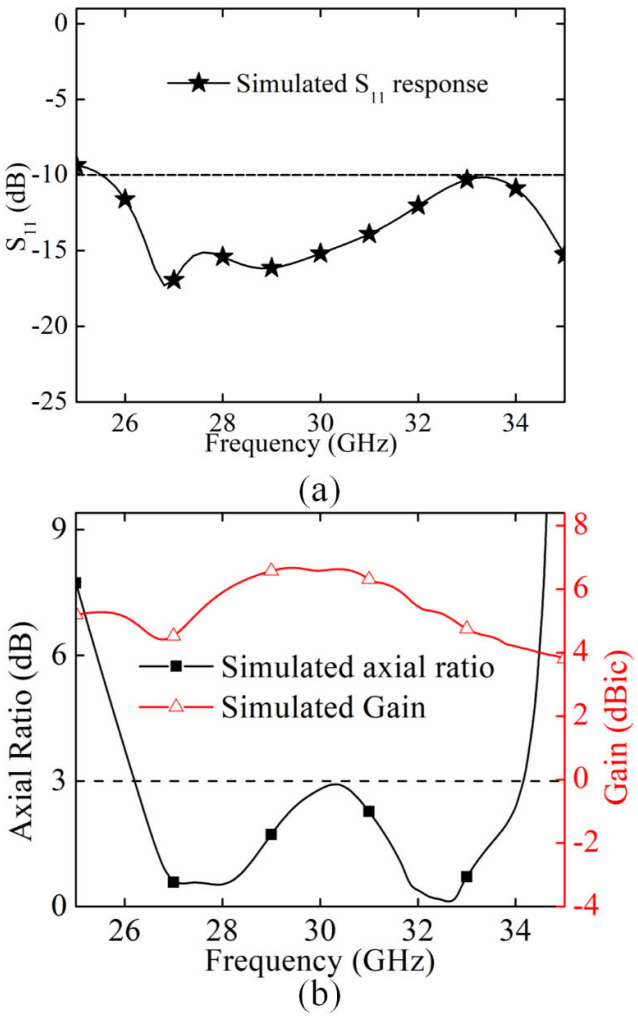

FIGURE 8. Simulated (a) S_{11}, (b) axial ratio and gain response of the proposed antenna element.

of an inductor (L_1) and a resistor (R_1) connected to the 50 Ω input port. The incident signal travels through the feedline and reaches to the top radiating patch through the cross-slot geometry and intermediate substrates. The cross-slot acts as a band pass filter and is denoted by a series combination of an inductor (L_2) and a capacitor (C_2). The intermediate substrates are modelled as equivalent transmission lines (Tx line 1 and 2). The metallic vias, engraved across the top dielectric, are presented as shunt inductances (L_3) in parallel with the Tx line 2. The trapezoidal patches are characterized by a radiation resistance (R_{rad}), an inductance (L_4), and a capacitance (C_1). The overall circuit is drawn in Advanced Design system (ADS) software and the circuit parameters are determined using curve tracing method, as follows: $L_1 = 0.7$ pH, $R_1 = 27.95$ Ω, $L_2 = 37.5$ pH, $C_2 = 30.0$ fF, $L_3 = 31.0$ pH, $R_{rad} = 64.0$ Ω, $C_1 = 8.2$ fF, and $L_4 = 3.14$ fH. A good agreement between the simulated HFSS response and the numerically calculated ADS result is observed in Fig.6.

D. PARAMETRIC ANALYSES

A few parametric analyses have been carried out to understand the contribution of various geometric dimensions in CP operation. The trapezoidal patches and their relative positions are the critical parameters to be studied. While reducing the trapezoidal patch widths (p_{l1}, p_{l2}) in the same proportion, the lower resonance (around 28 GHz) shifts towards the higher frequency, as shown in Fig. 7(a). The 32 GHz CP response depends on the combined effect of metallic vias, cross-slot, and patches, and any of their variations reflect a change in the AR value. When the relative position between the patches (d) is increased while keeping the cross-slot dimensions constant, the points of contact of the patches with the metallic vias are changed. Due to such a disturbance in the coupling, the CP behavior at the high frequency gets affected, as depicted in

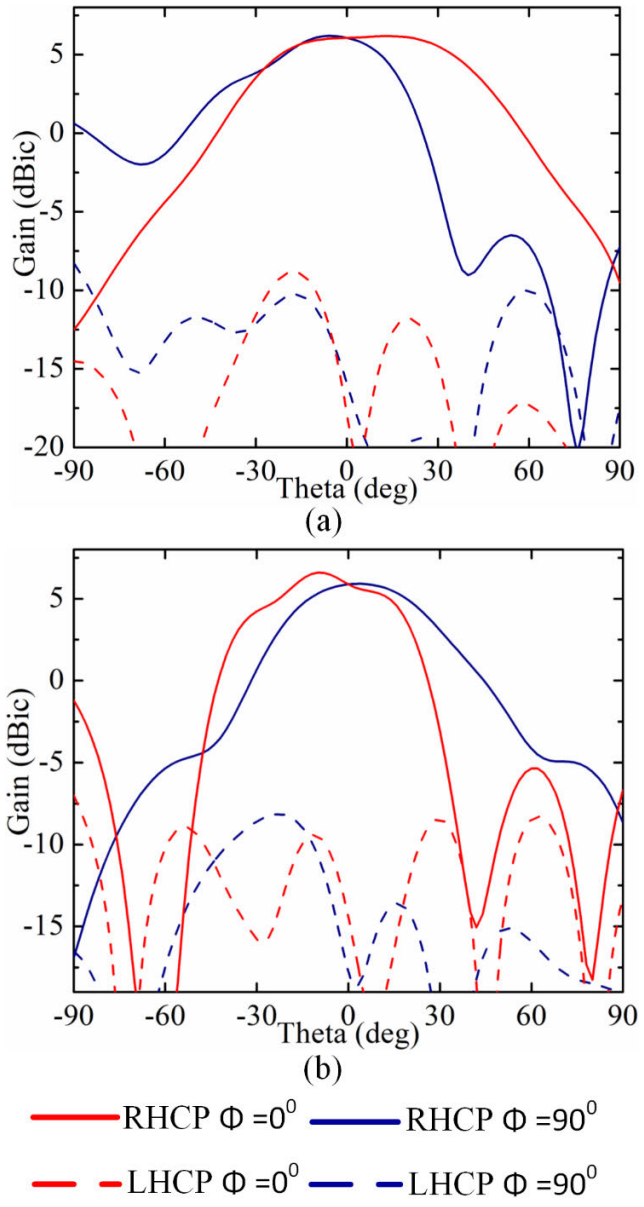

FIGURE 9. Radiation pattern of the antenna element at (a) 28 GHz, and (b) 32 GHz.

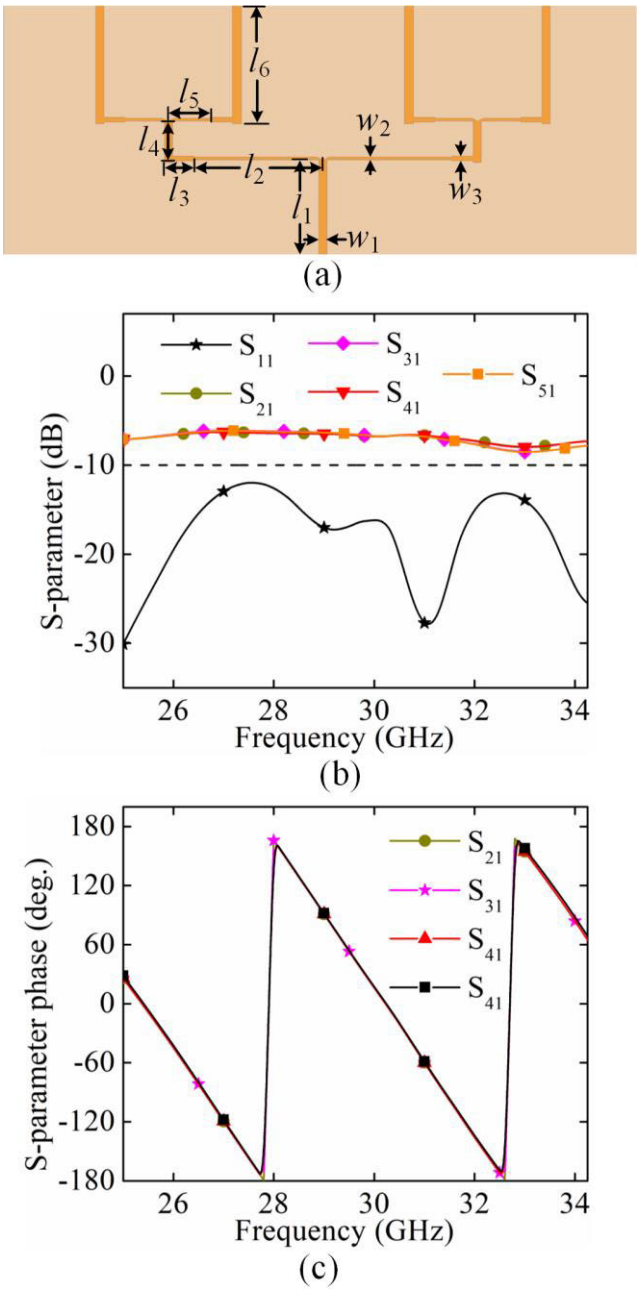

FIGURE 10. (a) Schematics of 1 × 4 power divider, with S-parameter responses: (b) amplitude, and (c) phase. The geometric dimensions are: $l_1 = 9.78$, $l_2 = 12.12$, $l_3 = 2$, $l_4 = 3.91$, $l_5 = 3.65$, $l_6 = 11.1$, $w_1 = 0.8$, $w_2 = 0.23$, $w_3 = 0.46$ (units: mm).

Fig. 7(b). The dimensions of different parameters are thereby optimized to obtain a good coupling and essential AR bandwidth throughout the CP band.

E. SIMULATED RESULTS

The simulated reflection coefficient (S_{11}) response of the proposed antenna is shown in Fig. 8(a) and a significantly level of impedance matching ($S_{11} < -10$ dB) is observed from 25.5 to 35.0 GHz (and even beyond 35.0 GHz; however, the same is not shown as that is outside the CP operating range). Thus the overall impedance bandwidth is computed as >31.40%. Fig. 8(b) depicts the simulated AR response and total gain in the broadside direction. The 3-dB AR response is observed from 26.20 to 34.16 GHz (having a fractional bandwidth of 26.38%), whereas a good gain of 5.6 ± 1.0 dBic has been achieved throughout the operating band. The simulated radiation patterns of the proposed antenna element in xz-plane and yz-plane at 28 GHz and 32 GHz are shown in Fig. 9, where the xz-plane and yz-plane are denoted by $\phi = 0°$ and $\phi = 90°$, respectively. The simulated responses deduce that the geometry emits RHCP-type EM wave in $+z$-direction depicting a broadside radiation. The slightly tilted radiation pattern responses can be attributed to the asymmetry in the antenna's geometry.

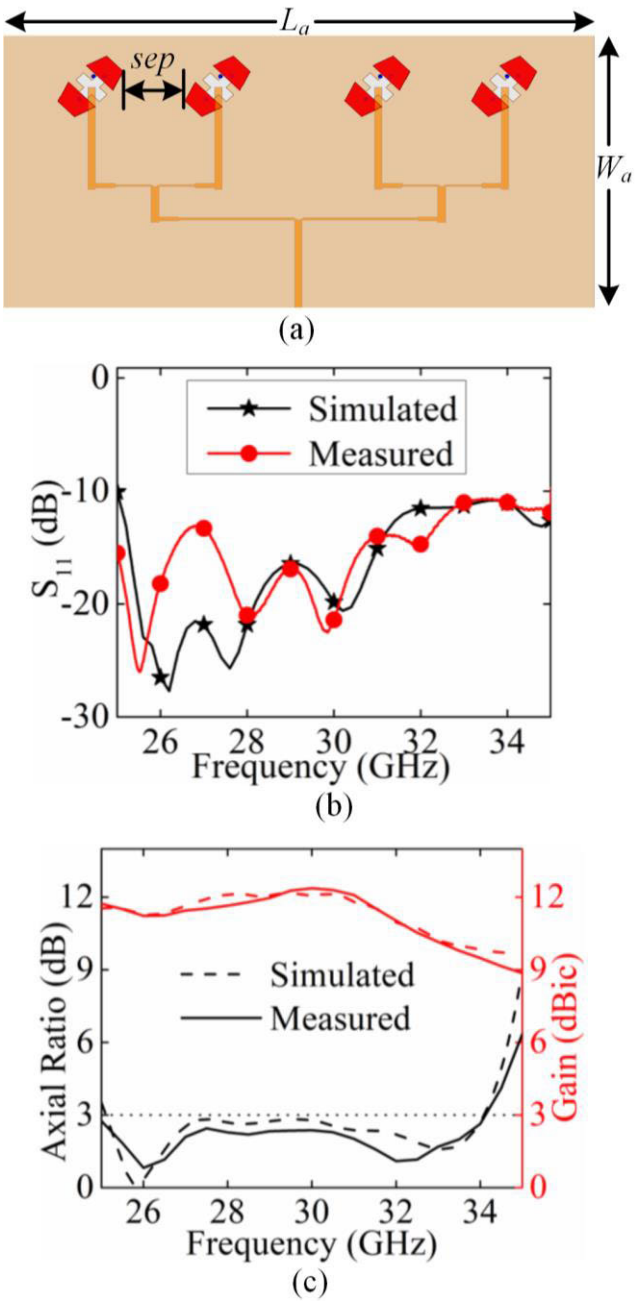

FIGURE 11. (a) Geometry of the proposed 1 × 4 antenna array having overall dimensions L_a = 60 mm, and W_a = 30 mm. Comparison between simulated and measured (b) S_{11}, and (c) axial ratio and gain response.

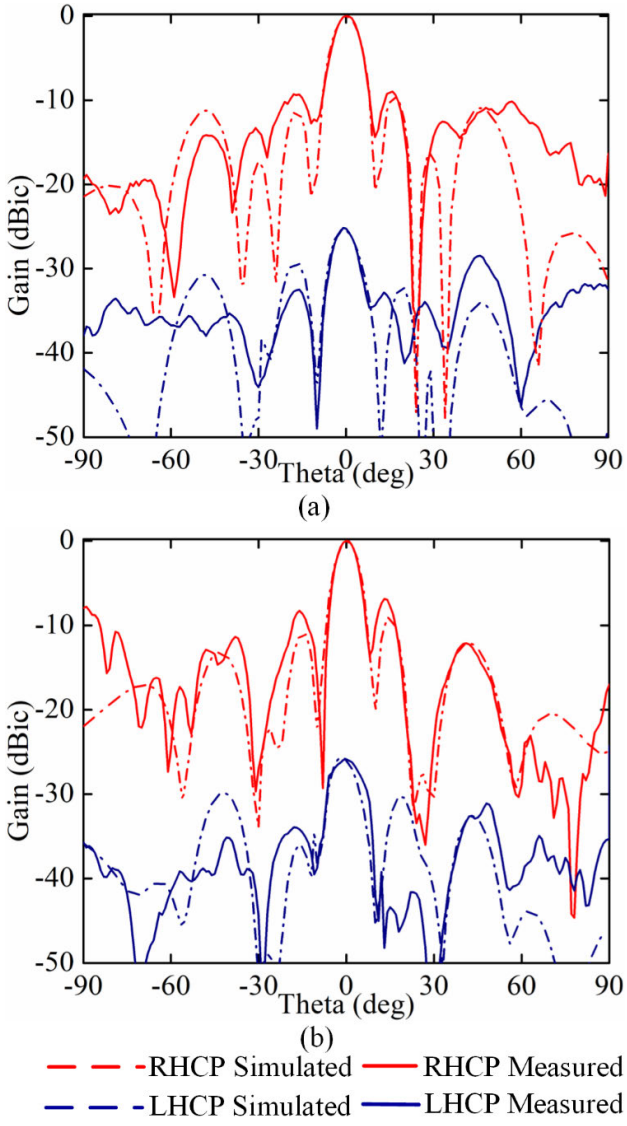

FIGURE 12. Radiation pattern of 1 × 4 antenna array in *xz*- plane ($\phi = 0°$) at (a) 28 GHz, and (b) 32 GHz.

III. ANTENNA ARRAY DESIGN

The use of high-gain antenna arrays is essential in mm-wave communication systems due to the significant free-space path loss and atmospheric loss in this frequency band compared to lower frequencies. To counteract this lrge propagation loss, a 1 × 4 antenna array is designed with the help of a power divider geometry, as illustrated in Fig. 10 (a). The power divider is made of a conventional corporate feed network, where the power from the input port is equally divided among the four output ports connected at the end of the feed geometry. The geometric dimensions are initially considered based on the quarter-wavelength conditions for attaining impedance matching and later optimized with a triangular cut at the divider point such that the entire operating bandwidth can be covered with the geometry. Figs. 10(b) and 10(c) depict the simulated magnitude and phase responses of the designed power divider, which confirms the operating behavior of the proposed design. The geometric dimensions of the divider are presented in the caption of Fig. 10.

Once the power divider is designed, the antenna array structure is realized by placing antenna elements at the end of the output ports, as shown in Fig. 11(a). As per the theoretical analysis, a separation of 5.06 mm (corresponding to $0.5\lambda_0$, where λ_0 is the wavelength at the center frequency 29.6 GHz of the CP bandwidth) is maintained between the adjacent elements to minimize the interference effect. A parametric

TABLE 1. Comparison with MM-Wave wideband CP antenna arrays.

Ref.	Frequency (GHz)	Imp. BW (-10 dB)	ARBW (3 dB)	Element numbers	Peak Gain (dBic)	Size (λ_0)	Thickness (λ_0)
[18]	11.7	25.10%	21.40%	4	15.10	2.06 × 2.79	0.23
[19]	28	28.60%	14.00%	16	18.20	6.80 × 4.50	0.21
[22]	60	14.10%	21.10%	16	19.50	4.80 × 4.80	0.49
[23]	29	29.60%	25.40%	16	20.32	10.20 × 8.70	0.098
[24]	29	13.80%	13.50%	16	15.83	N.A. × 3.28	0.098
[25]	28	17.39%	16.93%	4	12.00	5.14 × N.A.	0.15
Proposed work	**30**	**>33.33%**	**30.34%**	**4**	**12.16**	**5.92 × 2.96**	**0.035**

BW: Bandwidth, ARBW: Axial ratio BW, λ_0: free space wavelength at center frequency, N.A.: Not available

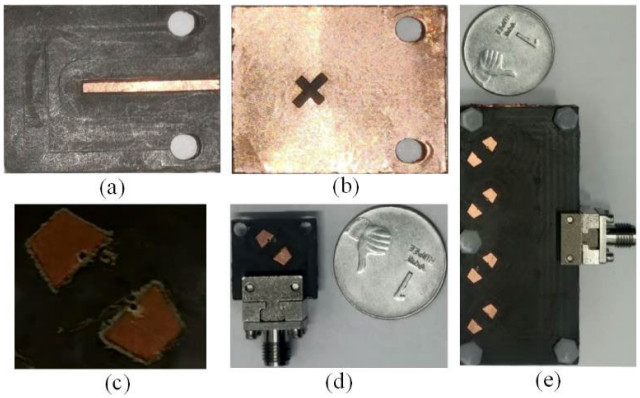

FIGURE 13. Fabricated prototypes of the proposed antenna structures. Single antenna: (a) bottom layer of the lower substrate, (b) bottom layer of the upper substrate, (c) top layer of upper substrate, and (d) complete antenna with connector. 1 × 4 antenna array: (e) top view.

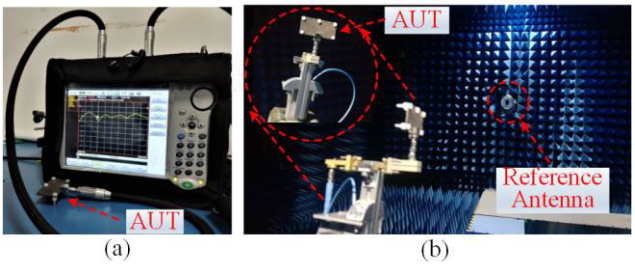

FIGURE 14. Photograph of the antenna measurement set up: (a) S_{11} measurement, and (b) far-field parameters measurement.

analysis has been carried out to investigate the impact of the separation distance between adjacent antenna elements on the antenna performance. It is observed that while changing the separation distance beyond 5.06 mm, a degradation in antenna performance occurs with respect to the gain and axial ratio. Thus, the antenna separation is maintained as 5.06 mm, resulting in an overall antenna array size of 60 mm × 30 mm ($5.92\lambda_0 \times 2.96\lambda_0$, where λ_0 is the wavelength at the center frequency 29.6 GHz). In Fig. 11(b), the simulated S_{11} is observed below -10 dB throughout the entire operating band (from 25 to 35 GHz and even beyond 35 GHz, thereby having a fractional bandwidth of >33.33%), whereas the AR is maintained over a bandwidth of 25.11 to 34.09 GHz (30.34%), as shown in Fig. 11(c). The overall gain is increased to 11.2 ± 1.0 dBic in the array geometry along with a peak gain of 12.16 dBic. This gain response is the total gain relative to a circularly polarized isotropic antenna (in dBic) in the broadside direction, specifically at theta (θ) = 0° and phi (ϕ) = 0°. The normalized radiation pattern in xz-plane ($\phi = 0°$) is plotted in Fig. 12. The results confirm that the antenna array radiates in the broadside direction as well.

Once the desired simulated responses are obtained for both the antenna element and antenna array, the geometries are thereafter fabricated. To create the metallic posts, drills are made at precise locations and later via metallization is done. The top and bottom layers are then stacked together by securely fastening nylon screws at multiple locations of the geometry. No adhesive is used in the stacking to avoid any possible change in the antenna performance. A high-precision 2.92 mm (K) end launch connector has been used to provide the signal in the geometry. The same connector model is used during full-wave simulation for matching purposes. Fig. 13 depicts the photograph of the fabricated prototypes, both single antenna and array network.

The Anritsu S820E vector network was used to measure the S_{11} parameter of the fabricated prototypes, while the axial ratio, gain, and normalized radiation pattern were measured inside an anechoic chamber using broadband horn antennas. Fig. 14 illustrates the images of the measurement setups, where the antenna under test (AUT) corresponds to the fabricated antenna array prototype. Instead of CP horn antennas, LP antennas are used in horizontal and vertical planes to capture the response for characterizing the radiation patterns [28], [29]. All the measured responses, as depicted in Figs. 11 and 12, exhibit good agreement between the simulated and measured responses. A slight variation is observed though, which can be accounted to the fabrication inaccuracy, presence of a small air gap between the stacked layers, and measurement difficulties at high frequency.

IV. CONCLUSION

In this letter, a wideband CP antenna array has been presented for 5G mm-wave communication. By exploiting the concept of trapezoidal patches, cross-slot, and metallic vias in the geometry, the CP operation has been broadened. The overall antenna structure is double-layered, and its array network exhibits a wide ARBW of 30.34% (26.38% for the single element), a large impedance bandwidth of >33.33% (>31.40% for the single element), and an average broadside gain of 11.2 dBic (5.6 dBic for the single element). A comparison is made with the recent CP antennas in Table 1 and the geometry shows a significant improvement in the ARBW performance and substrate height, while exhibiting commendable impedance bandwidth and operating gain with a limit in the total number of substrates (≤ 2). The prototypes are fabricated and the measured results show good resemblances with the simulated responses. The antenna array encompasses three 5G mm-wave allocated bands, namely n257 (26.5-29.5 GHz) and n261 (27.5-28.35 GHz) for both uplink and downlink, and covers a significant portion of the n258 band (24.25-27.5 GHz), thus providing an optimal solution for efficient 5G mm-wave communication across three frequency bands.

ACKNOWLEDGMENT

The authors would like to thank the Tokyo Institute of Technology, Japan, for providing antenna measurement facilities.

REFERENCES

[1] D. Lockie and D. Peck, "High-data-rate millimeter-wave radios," *IEEE Microw. Mag.*, vol. 10, no. 5, pp. 75–83, Aug. 2009.
[2] N. Hussain, M. Jeong, A. Abbas, and N. Kim, "Metasurface-based single-layer wideband circularly polarized MIMO antenna for 5G millimeter-wave systems," *IEEE Access*, vol. 8, pp. 130293–130304, 2020.
[3] M. Mantash and T. A. Denidni, "CP antenna array with switching-beam capability using electromagnetic periodic structures for 5G applications," *IEEE Access*, vol. 7, pp. 26192–26199, 2019.
[4] H. Jin, G. Q. Luo, W. Wang, W. Che, and K. Chin, "Integration design of millimeter-wave filtering patch antenna array with SIW four-way antiphase filtering power divider," *IEEE Access*, vol. 7, pp. 49804–49812, 2019.
[5] E. Baghernia, R. Movahedinia, and A. Sebak, "Broadband compact circularly polarized spiral antenna array fed by printed gap waveguide for millimeter-wave applications," *IEEE Access*, vol. 9, pp. 86–95, 2021.
[6] H. Ullah and F. A. Tahir, "A novel snowflake fractal antenna for dual-beam applications in 28 GHz band," *IEEE Access*, vol. 8, pp. 19873–19879, 2020.
[7] W. He, B. Xu, M. Gustafsson, Z. Ying, and S. He, "RF compliance study of temperature elevation in human head model around 28 GHz for 5G user equipment application: Simulation analysis," *IEEE Access*, vol. 6, pp. 830–838, 2018.
[8] P. Liu, X. Zhu, Y. Zhang, X. Wang, C. Yang, and Z. H. Jiang, "Patch antenna loaded with paired shorting pins and H-shaped slot for 28/38 GHz dual-band MIMO applications," *IEEE Access*, vol. 8, pp. 23705–23712, 2020.
[9] M. P. Singh, R. K. Jaiswal, K. V. Srivastava, and S. Ghosh, "A compact triband circularly polarized meander-loaded monopole antenna," *Microw. Opt. Technol. Lett.*, vol. 64, no. 2, pp. 382–388, Feb. 2022.
[10] M. P. Singh, R. K. Jaiswal, K. V. Srivastava, and S. Ghosh, "A miniaturized triple-band circularly polarized antenna using meander geometry," *J. Electromagn. Waves Appl.*, vol. 36, no. 2, pp. 228–236, Jan. 2022.
[11] A. Ludwig, "The definition of cross polarization," *IEEE Trans. Antennas Propag.*, vol. AP-21, no. 1, pp. 116–119, Jan. 1973.
[12] Y. Zhang, L. Pang, X. Liang, X. Liu, R. Chen, and J. Li, "Propagation characteristics of circularly and linearly polarized electromagnetic waves in urban macrocell scenario," *IEEE Trans. Veh. Technol.*, vol. 64, no. 1, pp. 209–222, Jan. 2015.
[13] C. C. Counselman, "Multipath-rejecting GPS antennas," *Proc. IEEE*, vol. 87, no. 1, pp. 86–91, Jan. 1999.
[14] E. Brookner, W. Hall, and R. Westlake, "Faraday loss for L-band radar and communications systems," *IEEE Trans. Aerosp. Electron. Syst.*, vol. AES-21, no. 4, pp. 459–469, Jul. 1985.
[15] S. S. Gao, Q. Luo, and F. Zhu, *Circularly Polarized Antennas*. Hoboken, NJ, USA: Wiley, 2013.
[16] S. S. Hesari and J. Bornemann, "Wideband circularly polarized substrate integrated waveguide endfire antenna system with high gain," *IEEE Antennas Wireless Propag. Lett.*, vol. 16, pp. 2262–2265, 2017.
[17] W. Lin, R. W. Ziolkowski, and T. C. Baum, "28 GHz compact omnidirectional circularly polarized antenna for device-to-device communications in the future 5G systems," *IEEE Trans. Antennas Propag.*, vol. 65, no. 12, pp. 6904–6914, Dec. 2017.
[18] W. Yang, W. Sun, H. Tang, and J. Chen, "Design of a circularly polarized dielectric resonator antenna with wide bandwidth and low axial ratio values," *IEEE Trans. Antennas Propag.*, vol. 67, no. 3, pp. 1963–1968, Mar. 2019.
[19] J. Wu, Y. J. Cheng, and Y. Fan, "Millimeter-wave wideband high-efficiency circularly polarized planar array antenna," *IEEE Trans. Antennas Propag.*, vol. 64, no. 2, pp. 535–542, Feb. 2016.
[20] Y. Yin and K. Wu, "Endfire circularly-polarized antipodal linearly tapered slot antenna fed by slotted width-tapered SIW," *IEEE Trans. Antennas Propag.*, vol. 70, no. 4, pp. 2411–2421, Apr. 2022.
[21] U. Ullah, M. Al-Hasan, S. Koziel, and I. B. Mabrouk, "A series inclined slot-fed circularly polarized antenna for 5G 28 GHz applications," *IEEE Antennas Wireless Propag. Lett.*, vol. 20, no. 3, pp. 351–355, Mar. 2021.
[22] Q. Zhu, K. Ng, and C. H. Chan, "Printed circularly polarized spiral antenna array for millimeter-wave applications," *IEEE Trans. Antennas Propag.*, vol. 65, no. 2, pp. 636–643, Feb. 2017.
[23] H. Xu, J. Zhou, K. Zhou, Q. Wu, Z. Yu, and W. Hong, "Planar wideband circularly polarized cavity-backed stacked patch antenna array for millimeter-wave applications," *IEEE Trans. Antennas Propag.*, vol. 66, no. 10, pp. 5170–5179, Oct. 2018.
[24] H. Al-Saedi, W. M. Abdel-Wahab, S. Gigoyan, R. Mittra, and S. Safavi-Naeini, "Ka-band antenna with high circular polarization purity and wide AR beamwidth," *IEEE Antennas Wireless Propag. Lett.*, vol. 17, no. 9, pp. 1697–1701, Sep. 2018.
[25] L. Wang and Z. Zilic, "Design of a Ka-band low-profile wideband circularly polarized magneto-electric dipole antenna with parasitic patches and its array," in *Proc. IEEE Asia–Pacific Microw. Conf. (APMC)*, Nov. 2021, pp. 305–307.
[26] H. Iwasaki, "A circularly polarized small-size microstrip antenna with a cross slot," *IEEE Trans. Antennas Propag.*, vol. 44, no. 10, pp. 1399–1401, Oct. 1996.
[27] K. Itoh and T. Adachi, "Novel circularly polarized antennas combining a slot with parasitic dipoles," in *Proc. Antennas Propag. Soc. Int. Symp.*, Quebec City, QC, Canada, Jun. 1980, pp. 52–55.
[28] W. L. Stutzman, *Polarization in Electromagnetic Systems*, 2nd ed. London, U.K.: Artech House, 2018.
[29] T. Tomura, Y. Saito, and J. Hirokawa, "8 × 2-element 60-GHz-band circularly polarized post-wall waveguide slot array antenna loaded with dipoles," *IEEE Access*, vol. 8, pp. 85950–85957, 2020.

MAHARANA PRATAP SINGH (Graduate Student Member, IEEE) was born in Mumbai, India, in 1991. He received the B.E. degree in electronics and telecommunication engineering from the University of Mumbai, India, in 2013, and the M.Tech. degree in electronics and communication engineering from NIT Hamirpur, India, in 2018. He is currently pursuing the Ph.D. degree in electrical engineering with the Indian Institute of Technology Indore, India. His research interests include microwave and millimeter wave circularly polarized antennas, reconfigurable antennas, diversity antennas, and substrate integrated waveguide structures.

JIRO HIROKAWA (Fellow, IEEE) was born in Tokyo, Japan, in 1965. He received the B.S., M.S., and D.E. degrees in electrical and electronic engineering from the Tokyo Institute of Technology (Tokyo Tech), Tokyo, in 1988, 1990, and 1994, respectively.

He was a Research Associate, from 1990 to 1996, and an Associate Professor, from 1996 to 2015, with Tokyo Tech, where he is currently a Professor. He was with the Antenna Group, Chalmers University of Technology, Gothenburg, Sweden, as a Postdoctoral Fellow, from 1994 to 1995. He has authored or coauthored more than 200 peer-reviewed journal articles and more than 600 international conference presentations. His current research interests include analyses, designs, the fabrication techniques of slotted waveguide array antennas, millimeter-wave, terahertz antennas, and beam-switching circuits.

Prof. Hirokawa is a fellow of IEICE. He received the IEEE AP-S Tokyo Chapter Young Engineer Award, in 1991, Young Engineer Award from IEICE, in 1996, Tokyo Tech Award for Challenging Research, in 2003, Young Scientist's Prize from the Minister of Education, Cultures, Sports, Science and Technology, Japan, in 2005, Best Paper Award, in 2007, the Best Letter Award, in 2009, from IEICE Communications Society, and IEICE Best Paper Award, in 2016 and 2018. He was the Chair of the Technical Program Committee of ISAP 2016. He was also the Chair of IEICE Technical Committee on Antennas and Propagation, from 2017 to 2019. He served as an Associate Editor for *IEICE Transactions on Communications*, from 1999 to 2003 and from 2004 to 2007. He also served as an associate editor, from 2013 to 2016, and a Track Editor for IEEE TRANSACTIONS ON ANTENNAS AND PROPAGATIONS, from 2016 to 2022.

SAPTARSHI GHOSH (Senior Member, IEEE) was born in West Bengal, India, in 1988. He received the B.E. degree in electronics and telecommunication engineering from IIEST, Shibpur, India, in 2009, and the M.Tech. and Ph.D. degrees in electrical engineering from IIT Kanpur, Kanpur, India, in 2013 and 2017, respectively.

After a postdoctoral researcher position with the Microwave Wireless Communication Laboratory, Chung-Ang University, Seoul, South Korea, he joined the Department of Electrical Engineering, Indian Institute of Technology Indore, India, in 2019, where he is currently an Assistant Professor. He has authored or coauthored more than 50 international journal articles and 70 conference papers during his research career. His current research interests include metamaterials, microwave absorbers, frequency selective surfaces, and millimeter-wave antennas.

Prof. received the Young Engineer Award from INAE, in 2022, IETE-IRSI (83) Young Scientist Award from IETE, in 2022, Motohisa Kanda Award from IEEE EMC Society, in 2022, Young Scientist Award from URSI-AT-AP-RASC, in 2022 and 2018, MIF Fellowship from Japan, in 2020, Young Innovative Student Projects Award from INAE, in 2018, and several best paper awards, in 2018, 2017, 2016, and 2013. He has also received outstanding reviewer awards from IEEE TAP and AWPL, in 2021 and 2019. He has been serving as an Associate Editor for IEEE ANTENNAS AND WIRELESS PROPAGATION LETTERS, since 2021.